Supplementary Information

Magnetic Exchange Interactions in Symmetric Lanthanide Dimetallics

Marcus J. Giansiracusa, Susan Al-Badran, Andreas K. Kostopoulos, George F. S. Whitehead, Eric J. L. McInnes, David Collison, Richard E. P. Winpenny and Nicholas F. Chilton

Table of Contents:

Table S1. Crystallographic information from single crystal XRD for **1**-**3**.

	(1)	(2)	(3)
Formula	$C_{40}H_{36}Er_2N_{10}O_{22}$	$C_{40}H_{36}Yb_2N_{10}O_{22}$	$C_{40}H_{36}Y_2N_{10}O_{22}$
Formula weight	1343.31	1354.87	1186.61
Temperature/K	150.02(10)	100(2)	100(2)
Crystal system	monoclinic	monoclinic	monoclinic
Space group	$P2_1/n$	$P2_1/n$	$P2_1/n$
a/Å	10.6199(8)	10.5837(3)	10.6108(3)
b/Å	18.1602(16)	18.0968(5)	18.1481(4)
c/Å	12.3952(10)	12.3473(3)	12.3809(4)
α/°	90	90	90
β/°	110.026(9)	110.098(2)	110.189(3)
γ/°	90	90	90
Volume/Å3	2246.0(3)	2220.88(11)	2237.64(11)
Z	2	2	2
ρcalcg/cm3	1.986	2.026	1.761
μ/mm-1	3.811	8.468	4.347
F(000)	1316	1324	1200
Crystal size/mm3	0.145 × 0.106 × 0.046	0.15 × 0.11 × 0.03	0.16 × 0.13 × 0.03
Radiation	MoKα (λ = 0.71073)	CuKα (λ = 1.54178)	CuKα (λ = 1.54184)
2Θ range for data collection/°	6.614 to 48.812	9.058 to 144.26	9.036 to 148.058
Index ranges	-9 ≤ h ≤ 12, -21 ≤ k ≤ 19, -13 ≤ l ≤ 14	-13 ≤ h ≤ 11, -22 ≤ k ≤ 19, -12 ≤ l ≤ 15	-12 ≤ h ≤ 13, -22 ≤ k ≤ 22, -15 ≤ l ≤ 14
Reflections collected	7700	12734	15465
Independent reflections	7700 [R_{int} = 0.0996, R_{sigma} = 0.3213]	4305 [R_{int} = 0.0419, R_{sigma} = 0.0407]	4451 [R_{int} = 0.0618, R_{sigma} = 0.0543]
Data/restraints/parameters	7700/240/337	4305/0/342	4451/0/336
Goodness-of-fit on F2	0.785	1.007	1.092
Final R indexes [I>=2σ (I)]	R1 = 0.0480, wR2 = 0.0862	R1 = 0.0269, wR2	R1 = 0.0417, wR2

		= 0.0603	= 0.1039
Final R indexes [all data]	R1 = 0.1001, wR2 = 0.0907	R1 = 0.0354, wR2 = 0.0631	R1 = 0.0507, wR2 = 0.1111
Largest diff. peak/hole / e Å-3	2.17/-1.24	1.08/-0.56	0.90/-0.80

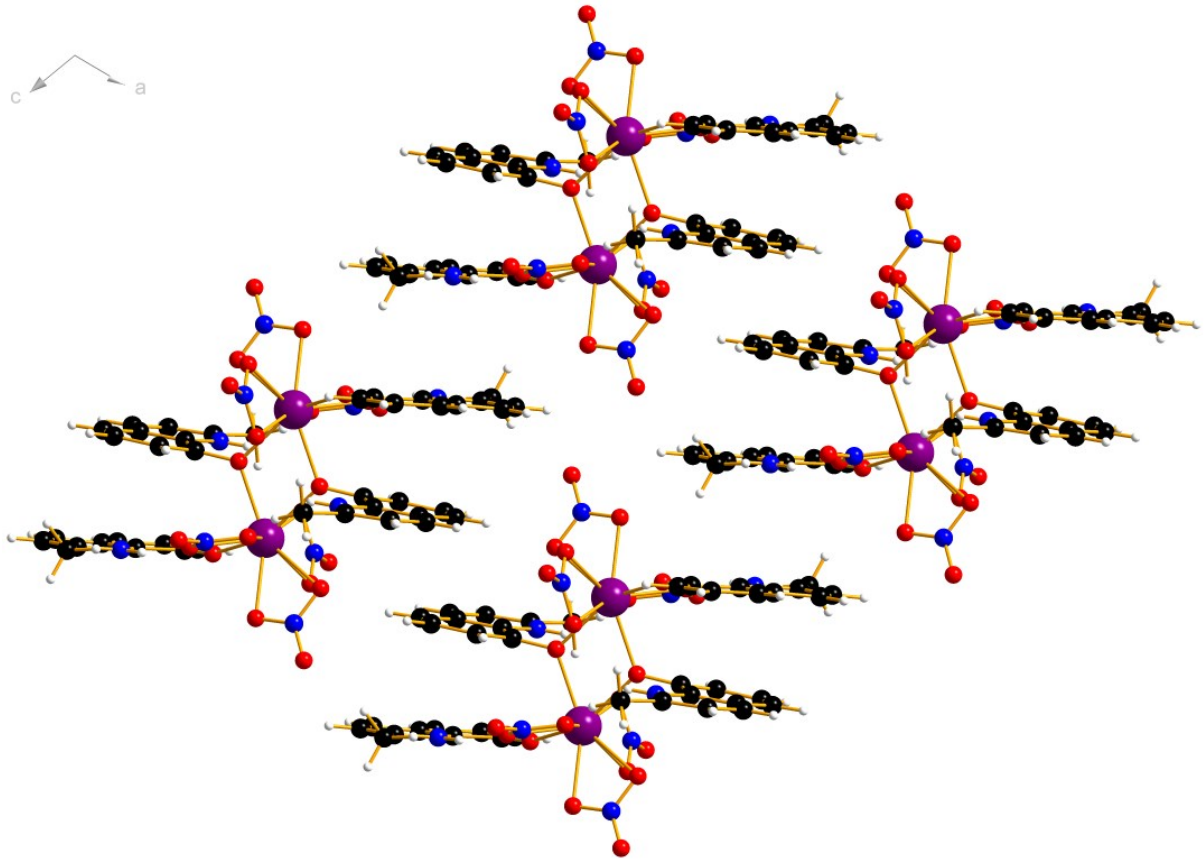

Figure S1. Crystal packing of **1** viewed along the *b* axis.

Table S2. Table of selected distances and angles for the series **1** – **3.**

	1 (Er)	2 (Yb)	3 (Y)
Ln1-Ln1'	3.8725(7)	3.8250(3)	3.8828(4)
Ln1-O1	2.3282(65)	2.3171(18)	2.3387(18)
Ln1-O1'	2.3342(46)	2.2887(22)	2.3294(25)
Ln1-O2	2.4597(79)	2.4440(31)	2.4598(31)
Ln1-O3	2.5060(73)	2.4668(26)	2.4911(24)
Ln1-O5	2.3970(53)	2.3766(22)	2.4106(22)
Ln1-O6	2.4887(66)	2.4744(30)	2.4971(30)
Ln1-O8	2.4051(67)	2.3888(29)	2.4071(23)
Ln1-O9	2.4861(75)	2.4786(26)	2.4952(26)
Ln1-O11	2.1887(77)	2.1680(28)	2.2012(25)
Ln1-O1-Ln1'	112.3(2)	112.29(8)	112.56(9)

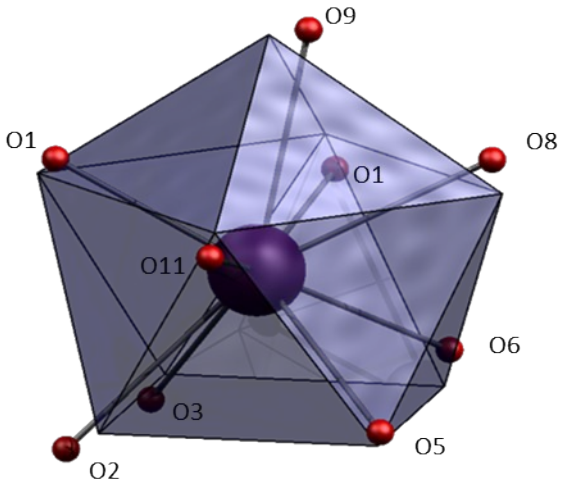

Figure S2. The "Spherical Capped Square Antiprism" coordination polyhedron around the Er site in the structure of **1.**

Table S3. SHAPE result for the Er ion environment in **1**, showing the lowest residue for a spherical capped square antiprism.

EP-9	OPY-9	HBPY-9	JTC-9	JCCU-9	CCU-9	JCSAPR-9	CSAPR-9	JTCTPR-9
35.058	20.41	17.432	14.893	10.591	9.22	2.975	2.082	4.023

EP-9	1 D9h	Enneagon
OPY-9	2 C8v	Octagonal pyramid
HBPY-9	3 D7h	Heptagonal bipyramid
JTC-9	4 C3v	Johnson triangular cupola J3
JCCU-9	5 C4v	Capped cube J8
CCU-9	6 C4v	Spherical-relaxed capped cube
JCSAPR-9	7 C4v	Capped square antiprism J10
CSAPR-9	8 C4v	Spherical capped square antiprism
JTCTPR-9	9 D3h	Tricapped trigonal prism J51

Table S4. Single ion magnetic values to compare RT values of the Ln_2 dimers.

Ion	J	g_J	$\chi_M T$	Exp Ln_2 RT $\chi_M T$
Er^{III}	15/2	6/5	22.96	22.89
Yb^{III}	7/2	8/7	5.14	5.02

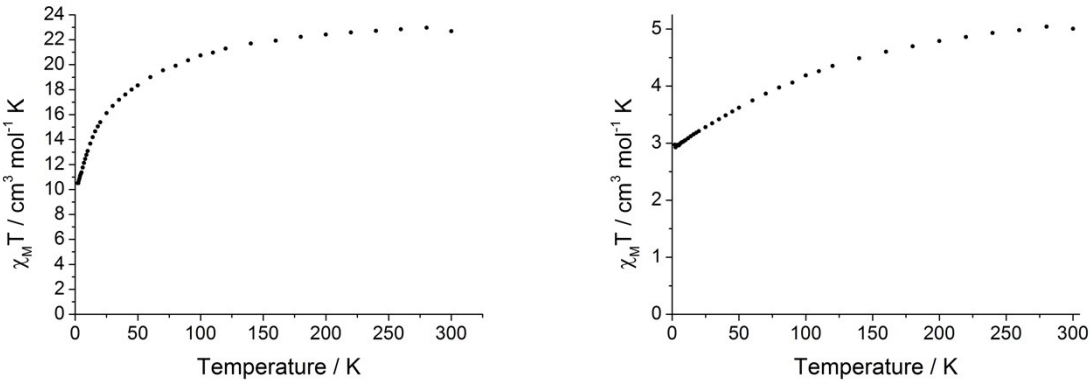

Figure S3. Magnetic susceptibility measurements $\chi_M T$ for **1** (**left**) and **2** (**right**) from 1.8 to 300 K.

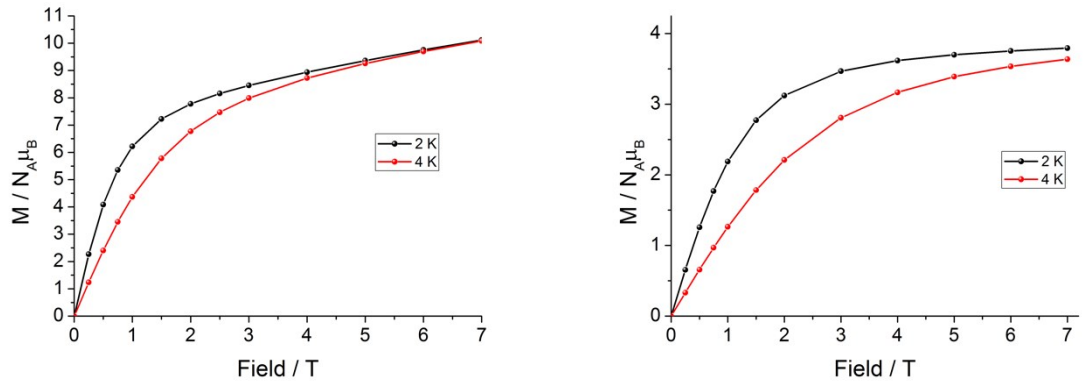

Figure S4. Molar magnetization for **1** (**left**) and **2** (**right**) at 2 and 4 K.

Table S5. CASSCF-SO calculations of **1** performed using the reported crystal structure on a single ion site, with the wavefunction decomposition performed in the basis of the ground Kramer's doublet.

Energy (K)	Energy (cm^{-1})	g_3	g_2	g_1	Angle (°)	Wavefunction
0	0	1.90	3.19	12.80	--	36.8|±15/2⟩, 12.8|±13/2⟩, 13.7|±11/2⟩, 17.5|±9/2⟩, 11.7|±7/2⟩, 2.9|±5/2⟩, 1.5|±3/2⟩, 3.1|±1/2⟩
41	29	2.35	6.06	7.68	83.76	9.6|±15/2⟩, 5.1|±13/2⟩, 2.4|±11/2⟩, 24.6|±9/2⟩, 21.7|±7/2⟩, 22.7|±5/2⟩, 9.4|±3/2⟩, 4.5|±1/2⟩
109	75	1.64	2.34	11.89	10.62	35.9|±15/2⟩, 2.7|±13/2⟩, 35.0|±11/2⟩, 6.6|±9/2⟩, 12.9|±7/2⟩, 1.6|±5/2⟩, 1.3|±3/2⟩, 3.9|±1/2⟩
162	113	3.09	5.08	8.16	39.24	1.6|±15/2⟩, 21.1|±13/2⟩, 12.0|±11/2⟩, 20.5|±9/2⟩, 12.1|±7/2⟩, 14.7|±5/2⟩, 13.1|±3/2⟩, 4.9|±1/2⟩
231	161	1.62	2.71	7.76	54.60	6.4|±15/2⟩, 27.7|±13/2⟩, 3.8|±11/2⟩, 9.3|±9/2⟩, 17.7|±7/2⟩, 13.7|±5/2⟩, 20.7|±3/2⟩, 0.7|±1/2⟩
285	198	1.93	6.14	9.89	9.24	7.8|±15/2⟩, 26.1|±13/2⟩, 23.7|±11/2⟩, 9.2|±9/2⟩, 10.8|±7/2⟩, 15.5|±5/2⟩, 3.2|±3/2⟩, 3.7|±1/2⟩
370	257	0.20	1.99	11.32	81.63	1.2|±15/2⟩, 1.5|±13/2⟩, 7.9|±11/2⟩, 10.9|±9/2⟩, 7.6|±7/2⟩, 12.3|±5/2⟩, 14.0|±3/2⟩, 44.7|±1/2⟩
470	327	0.74	2.69	15.22	84.14	0.7|±15/2⟩, 3.0|±13/2⟩, 1.5|±11/2⟩, 1.5|±9/2⟩, 5.5|±7/2⟩, 16.6|±5/2⟩, 36.8|±3/2⟩, 34.5|±1/2⟩

Table S6. CASSCF-SO calculations of **2** performed using the reported crystal structure on a single ion site, with the wavefunction decomposition performed in the basis of the ground Kramer's doublet.

Energy (K)	Energy (cm^{-1})	g_3	g_2	g_1	Angle (°)	Wavefunction
0	0	0.68	1.17	7.34	--	91.0 |±7/2⟩, 1.8|±5/2⟩, 5.2|±3/2⟩, 1.9|±1/2⟩
321	223	1.58	3.44	3.87	66.85	4.4|±7/2⟩, 60.2|±5/2⟩, 22.5|±3/2⟩, 12.9|±1/2⟩
445	309	0.01	0.91	6.60	86.78	2.8|±7/2⟩, 21.7|±5/2⟩, 53.6|±3/2⟩, 21.9|±1/2⟩
632	439	0.70	0.91	7.42	82.55	1.8|±7/2⟩, 16.3|±5/2⟩, 18.7|±3/2⟩, 63.2|±1/2⟩

Equation S1-3. Rotation convention for PHI listed below.

$$\bar{\bar{g}}_i = \bar{\bar{R}} \cdot \begin{bmatrix} g_1 & 0 & 0 \\ 0 & g_2 & 0 \\ 0 & 0 & g_3 \end{bmatrix} \cdot \bar{\bar{R}}^T \quad \text{(S1)}$$

$$\bar{\bar{R}} = \begin{bmatrix} \cos\alpha & -\sin\alpha & 0 \\ \sin\alpha & \cos\alpha & 0 \\ 0 & 0 & 1 \end{bmatrix} \begin{bmatrix} \cos\beta & 0 & \sin\beta \\ 0 & 1 & 0 \\ -\sin\beta & 0 & \cos\beta \end{bmatrix} \begin{bmatrix} \cos\gamma & -\sin\gamma & 0 \\ \sin\gamma & \cos\gamma & 0 \\ 0 & 0 & 1 \end{bmatrix} \quad \text{(S2)}$$

$$\bar{\bar{J}} = \bar{\bar{R}} \cdot \begin{bmatrix} J_x & 0 & 0 \\ 0 & J_y & 0 \\ 0 & 0 & J_z \end{bmatrix} \cdot \bar{\bar{R}}^T \quad \text{(S3)}$$

Equation S4-6. Rotation convention for Easyspin listed below.

$$\bar{\bar{g}}_i = \bar{\bar{R}}^T \cdot \begin{bmatrix} g_1 & 0 & 0 \\ 0 & g_2 & 0 \\ 0 & 0 & g_3 \end{bmatrix} \cdot \bar{\bar{R}} \quad \text{(S4)}$$

$$\bar{\bar{R}} = \begin{bmatrix} \cos\gamma & \sin\gamma & 0 \\ -\sin\gamma & \cos\gamma & 0 \\ 0 & 0 & 1 \end{bmatrix} \begin{bmatrix} \cos\beta & 0 & -\sin\beta \\ 0 & 1 & 0 \\ \sin\beta & 0 & \cos\beta \end{bmatrix} \begin{bmatrix} \cos\alpha & \sin\alpha & 0 \\ -\sin\alpha & \cos\alpha & 0 \\ 0 & 0 & 1 \end{bmatrix} \quad \text{(S5)}$$

$$\bar{\bar{J}} = \bar{\bar{R}}^T \cdot \begin{bmatrix} J_x & 0 & 0 \\ 0 & J_y & 0 \\ 0 & 0 & J_z \end{bmatrix} \cdot \bar{\bar{R}} \quad \text{(S6)}$$

Equation S7. Dipolar interaction matrix (in cm^{-1}) from equation 2 for **1**, used to give the simulations in Figure S5 represented in the *g* frame (**left**, here g_1 represents x, g_2 represents y and g_3 represents z) and the final model reference frame (**right**, here z is defined along the Er-Er vector, and J_{xx} forms a 22.5 ° angle with the bridging oxo bond).

$$\begin{pmatrix} 0.045 & 0.039 & 0.048 \\ 0.039 & -0.066 & 0.026 \\ 0.048 & 0.026 & -0.397 \end{pmatrix} \qquad \begin{pmatrix} -0.316 & -0.156 & -0.092 \\ -0.156 & -0.055 & 0.031 \\ -0.092 & 0.031 & -0.047 \end{pmatrix}$$

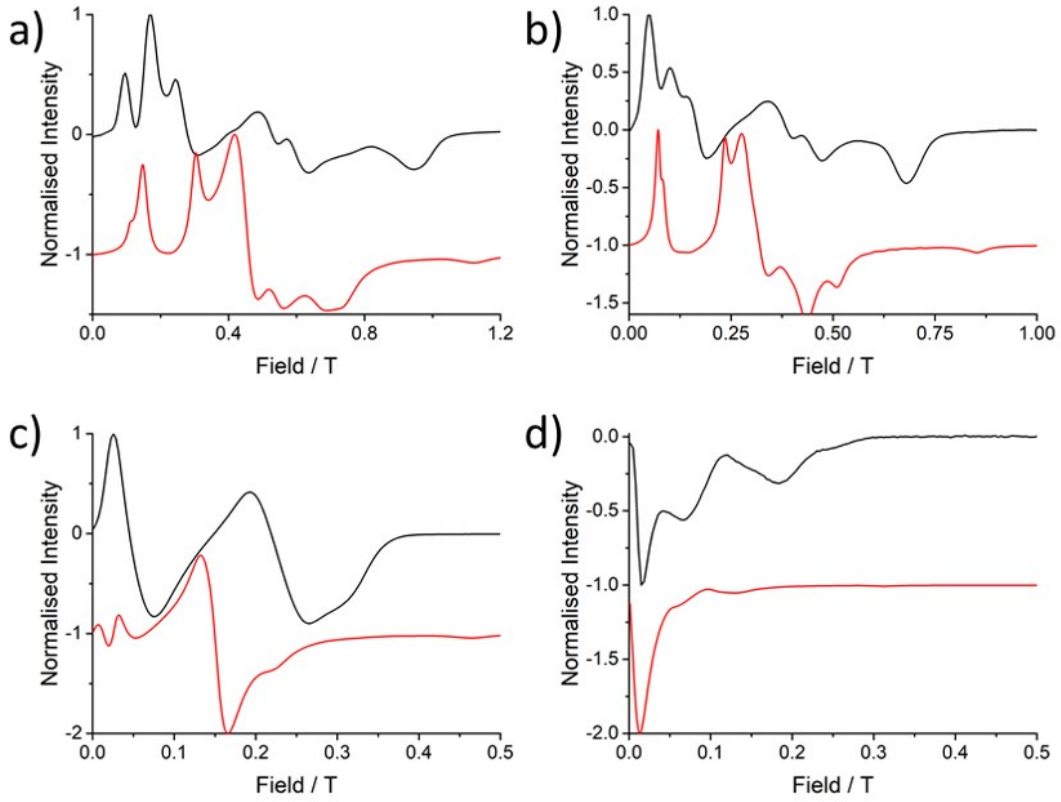

Figure S5. EPR simulations for **1** performed at each frequency **a)** *Q*-band (33.970818 GHz), **b)** *K*-band (23.791 GHz), **c)** *X*-band (9.37198 GHz) and **d)** *S*-band (3.87285 GHz) using the dipole interaction matrix equation S7 and equation 3 in the main text.

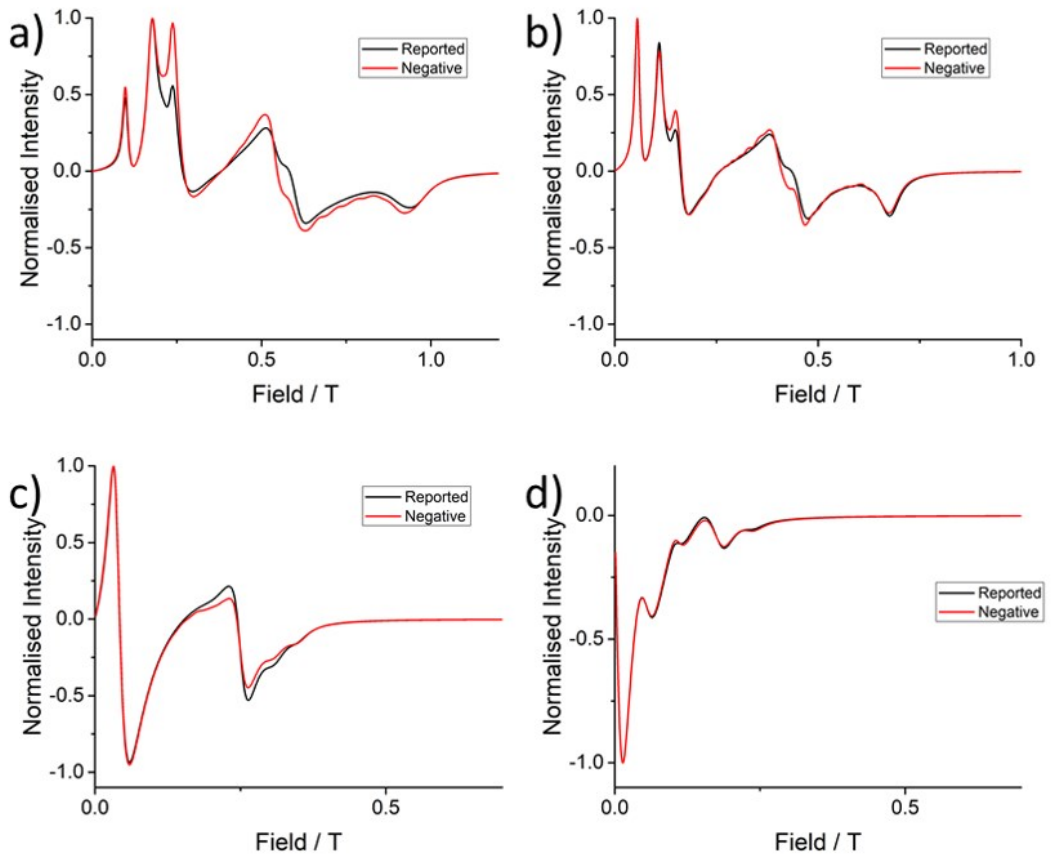

Figure S6. EPR simulations of **1** at each frequency **a)** *Q*-band (33.970818 GHz), **b)** *K*-band (23.791 GHz), **c)** *X*-band (9.37198 GHz) and **d)** *S*-band (3.87285 GHz) highlighting the effect of inverting the sign of the reported exchange ($\bar{\bar{J}}$ = black) to give the negative interaction matrix ($^{-}\bar{\bar{J}}$ = red = (-0.31, 0.24, 0.07)).

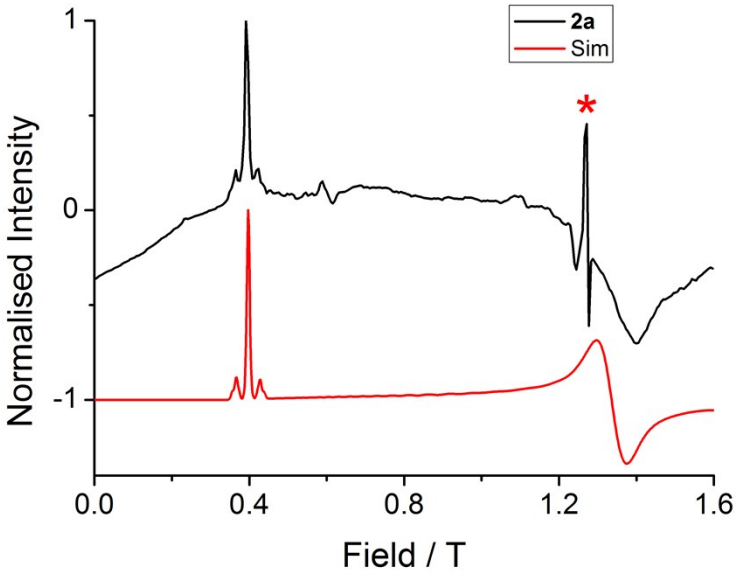

Figure S7. Q-Band EPR measurement collected at 5 K at 33.955792 GHz on the 2 % diluted **2a** analogue (black) with the fitted spectrum (red) obtained using Easyspin to account for the Yb hyperfine splitting. Asterisks for impurity signal at g = 2 which is prominent due to weak signal from diluted sample.

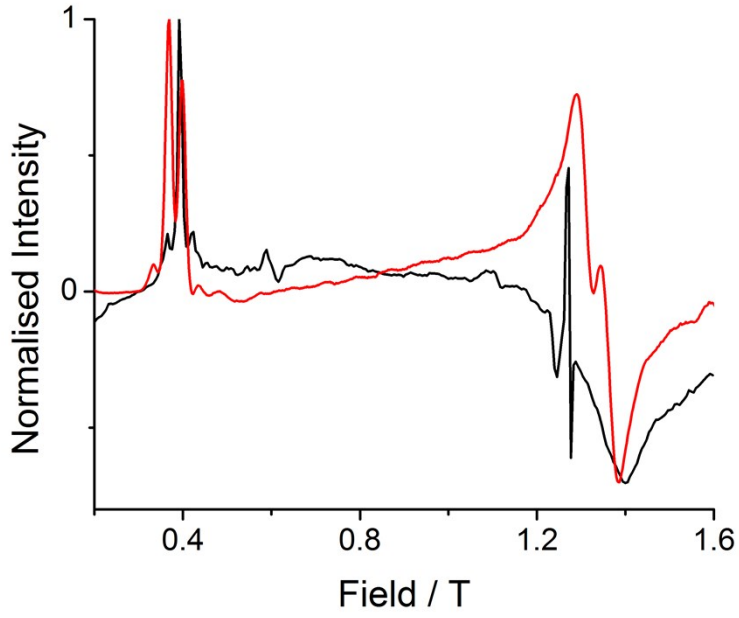

Figure S8. Comparison of **2a** (black) at 5 K at 33.955792 GHz and **2** (red) 5 K at 34.092351 GHz *Q*-band EPR spectra.

Equation S8. Dipolar interaction matrix (in cm^{-1}) from equation 2 for **2**, used to give the simulations in Figure S9 represented in the *g* frame (**left**, here g_1 represents x, g_2 represents y and g_3 represents z) and the final model reference frame (**right**, here z is defined along the Yb-Yb vector as shown in figure S16).

$$\begin{pmatrix} 0.001 & 0.007 & 0.003 \\ 0.007 & 0.007 & 0.009 \\ 0.003 & 0.009 & -0.142 \end{pmatrix} \qquad \begin{pmatrix} -0.073 & -0.074 & -0.008 \\ -0.074 & -0.060 & -0.017 \\ -0.008 & -0.017 & -0.001 \end{pmatrix}$$

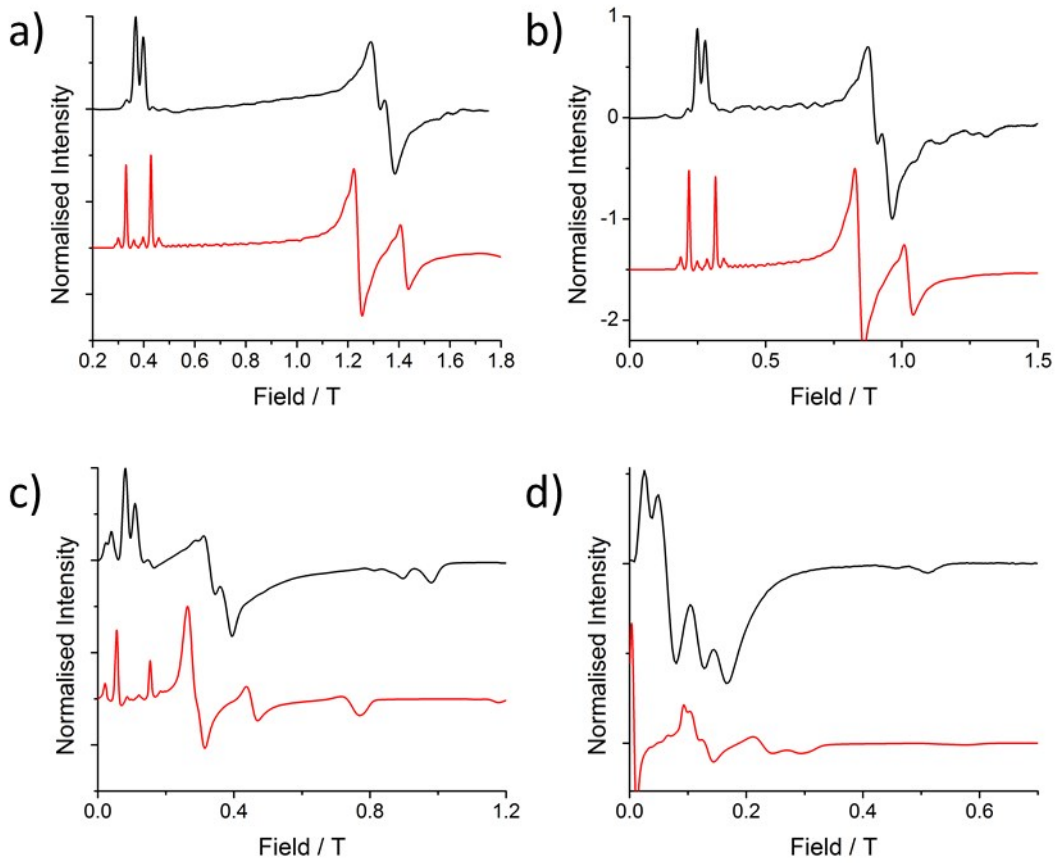

Figure S9. EPR simulations for **2** at each frequency **a)** *Q*-band (34.092351 GHz), **b)** *K*-band (23.870 GHz), **c)** *X*-band (9.374342 GHz) and **d)** *S*-band (3.875789 GHz) performed using the dipole interaction matrix equation S8 and equation 4 in the main text.

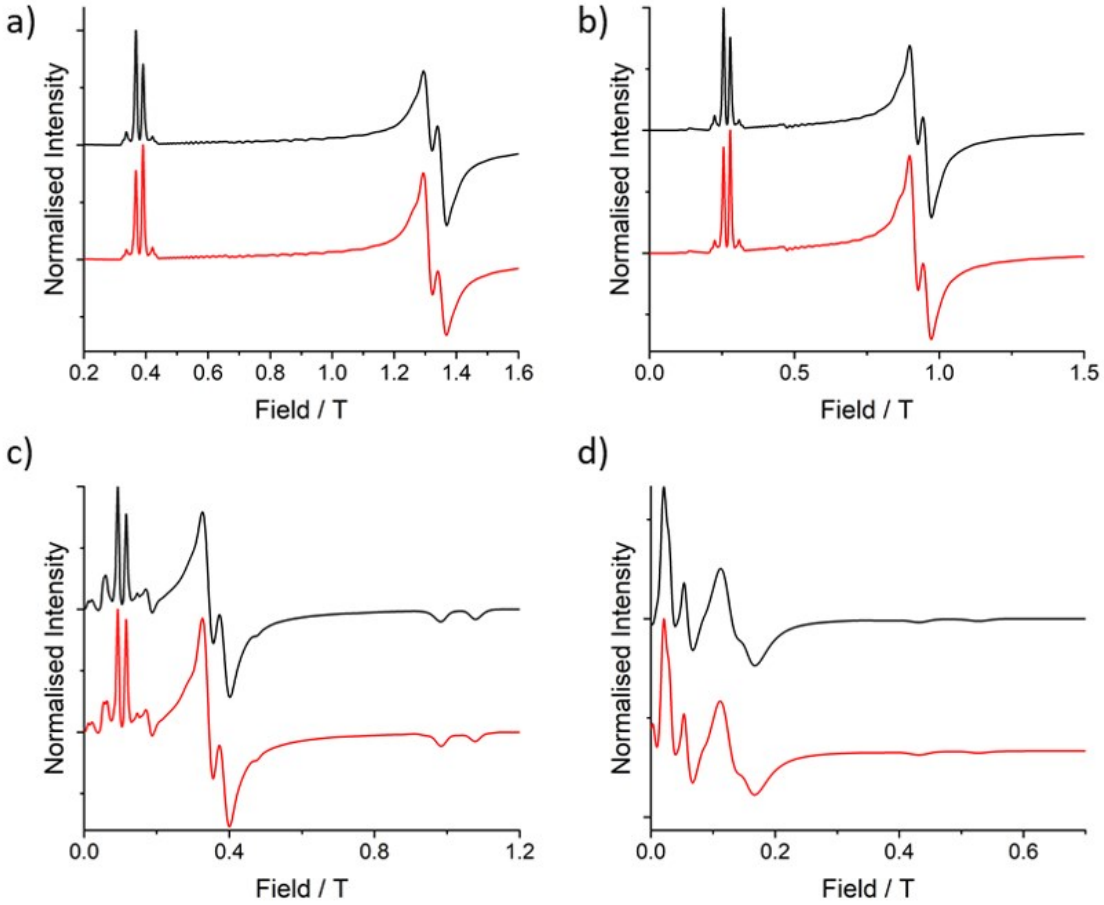

Figure S10. EPR simulations of **2** at each frequency **a)** *Q*-band (34.092351 GHz), **b)** *K*-band (23.870 GHz), **c)** *X*-band (9.374342 GHz) and **d)** *S*-band (3.875789 GHz) highlighting the effect of inverting the sign ($-\bar{\bar{J}}$ = red) of the reported exchange interaction matrix in the manuscript ($\bar{\bar{J}}$ = black).

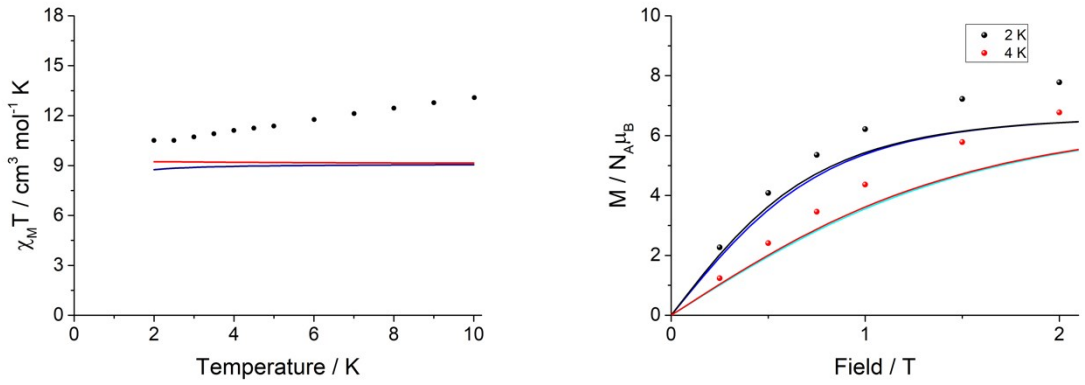

Figure S11. Susceptibility (**left**) and magnetisation (**right**) low temperature data for (**1**), compared with the exchange model simulation ($\bar{J}$ = red/black line, $-\bar{J}$ = (-0.31, 0.25, 0.07) = blue/cyan line).

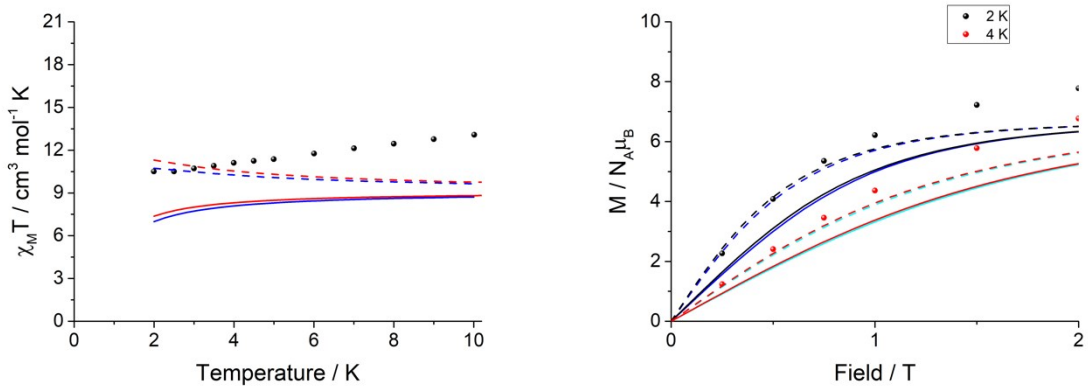

Figure S12. Susceptibility (**left**) and magnetisation (**right**) low temperature data for (**1**), compared with the previously reported exchange model simulation with the inclusion of a $+n\bar{J}$ component ranging from -0.5 to +1 cm^{-1}, showing the upper (**dashed**) and lower (**solid**) bound values for a reasonable reproduction of the low temperature magnetic data (using $\bar{J}$ = red/black and $-\bar{J}$ = blue/cyan). $\bar{J}_{lower}$ = (-0.19, -0.75, -0.57), $\bar{J}_{upper}$ = (1.31, 0.75, 0.93), $-\bar{J}_{lower}$ = (-0.81, -0.25, -0.43) and $-\bar{J}_{upper}$ = (0.69, 1.25, 1.07).

Table S7. Resultant exchange coupled states from the two interacting S_{eff} = 1/2 spins for **1** showing the energy spectrum, state contributions and average magnetic moment matrix elements between each state. NOTE state 3 at 0.24 cm^{-1} is the S_{eff} = 0 state which has zero transition probability with the other states.

Energy	**(cm^{-1})**	0.00	0.18	0.24	0.56
$m_{S(1)}$	$m_{S(2)}$				
-0.5	**-0.5**	34.0%	48.8%	0.0%	17.3%
-0.5	**0.5**	16.0%	1.2%	50.0%	32.7%
0.5	**-0.5**	16.0%	1.2%	50.0%	32.7%
0.5	**0.5**	34.0%	48.8%	0.0%	17.3%

Transition Probability	**1**	**2**	**3**	**4**
1		27.32		3.72
2	27.32			17.49
3				
4	3.72	17.49		

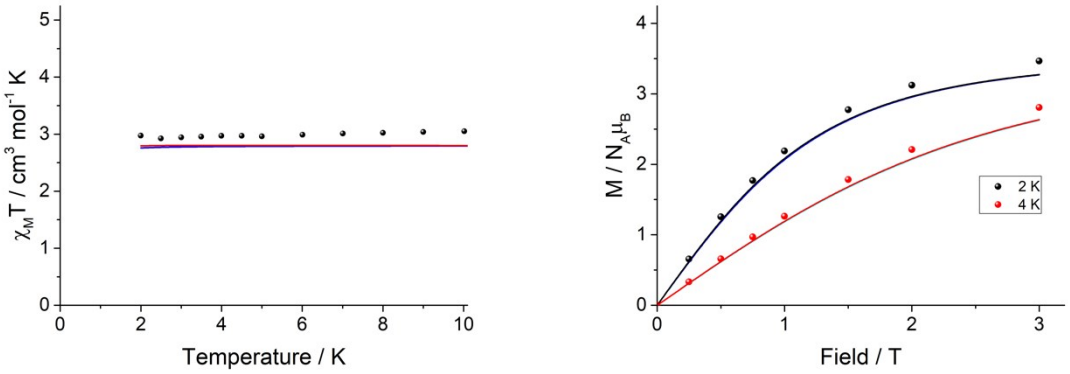

Figure S13. Susceptibility (**left**) and magnetisation (**right**) low temperature data for (**2**), compared with the exchange model simulation ($\bar{J}$ = red/black line, $-\bar{J}$ = (-0.023, -0.023, 0.047) = blue/cyan line).

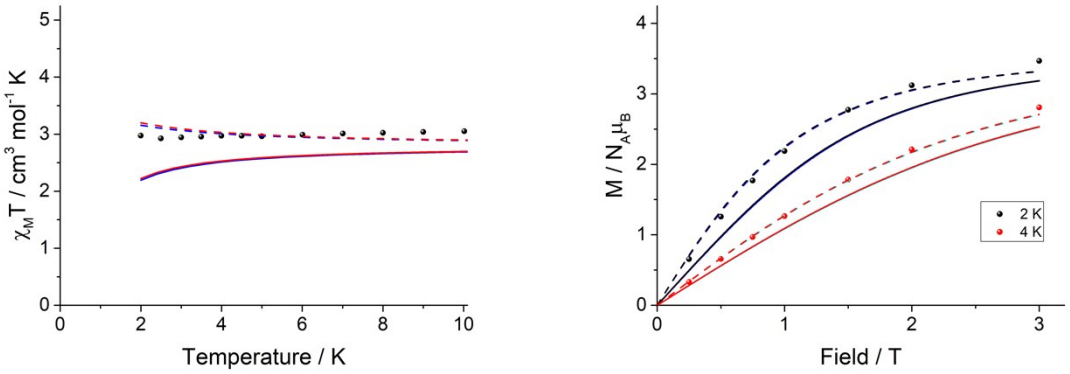

Figure S14. Susceptibility (**left**) and magnetisation (**right**) low temperature data for (**2**), compared with the previously reported exchange model simulation with the inclusion of a $+n\bar{J}$ component ranging from -0.5 to 0.5 cm^{-1}, showing the upper (**dashed**) and lower (**solid**) bound values for a reasonable reproduction of the low temperature magnetic data (using $\bar{J}$ = red/black and $-\bar{J}$ = blue/cyan). $\bar{J}_{lower}$ = (-0.477, -0.477, -0.547), $\bar{J}_{upper}$ = (0.523, 0.523, 0.453), $-\bar{J}_{lower}$ = (-0.523, -0.523, -0.453) and $-\bar{J}_{upper}$ = (0.477, 0.477, 0.547).

Table S8. Resultant exchange coupled states from the two interacting S_{eff} = 1/2 spins for 2 showing the energy spectrum, state contributions and average magnetic moment matrix elements between each state. NOTE state 2 at 0.05 cm^{-1} is the S_{eff} = 0 state which has zero transition probability with the other states.

Energy	**(cm^{-1})**	0.00	0.05	0.07	0.07
$m_{S(1)}$	$m_{S(2)}$				
-0.5	**-0.5**	49.5%	0.0%	48.5%	2.0%
-0.5	**0.5**	0.5%	50.0%	0.5%	49.0%
0.5	**-0.5**	0.5%	50.0%	0.5%	49.0%
0.5	**0.5**	49.5%	0.0%	50.5%	0.0%

Transition Probability	**1**	**2**	**3**	**4**
1			13.40	0.88
2				
3	13.40			0.89
4	0.88		0.89	

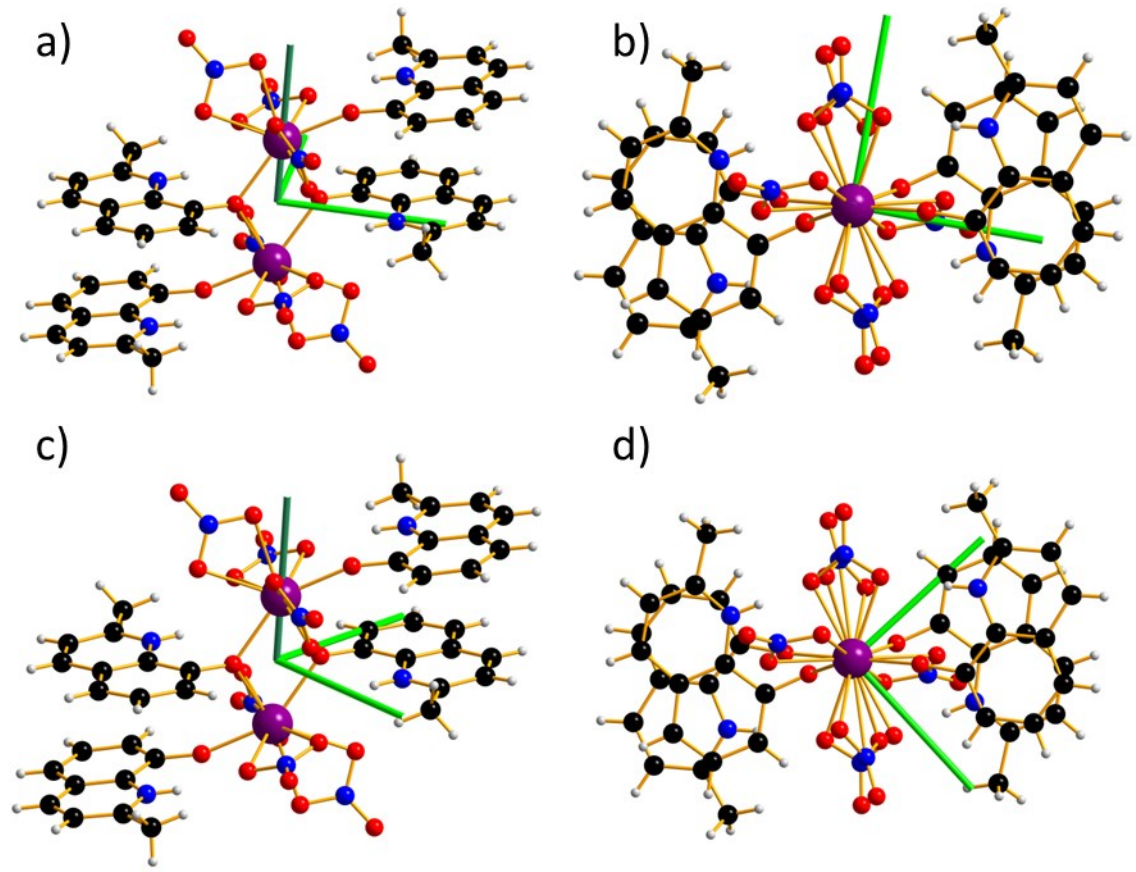

Figure S15. a) Side view and **b)** top view of exchange reference frame for **1** with Euler angle γ = 0 ° prior to fitting cycles and **c)** side view and **d)** top view of exchange reference frame following fitting cycles with γ = 36 °. Dark green represents the J_{zz} direction.

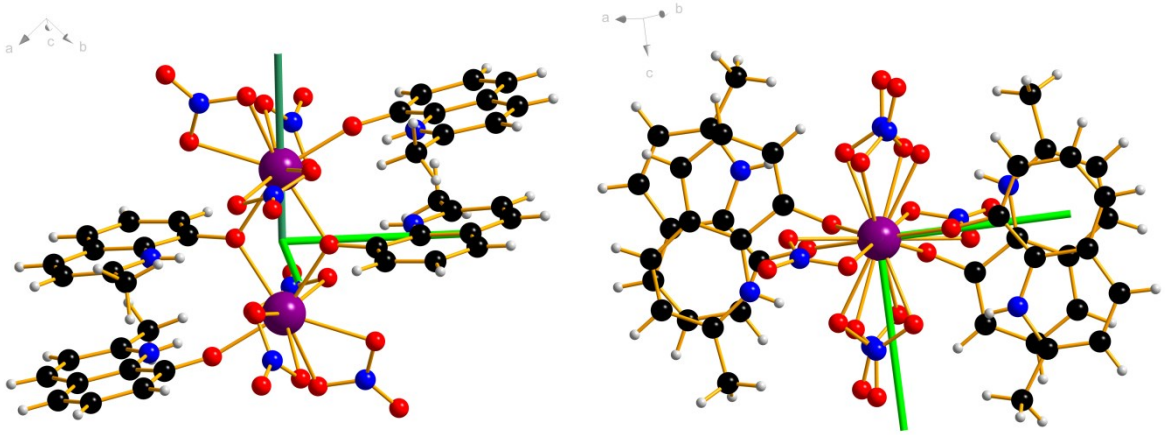

Figure S16. Left) side view and **right)** top view of exchange reference frame for **2** with Euler angle γ = 0 °. Dark green represents the J_{zz} direction.

Table S9. Fitted parameters for **1** after shifting of g-frame relative to exchange frame by ±5° and ±10°. Note that fitted centre values are identical for all using ±5°.

	α+5°, β+5°	**α+5°, β-5°**	**α-5°, β+5°**	**α-5°, β-5°**
J_x-J_z (cm^{-1})	0.38	0.38	0.38	0.38
J_y-J_z (cm^{-1})	-0.18	-0.18	-0.18	-0.18
γ_{ex} (°)	35	35	35	35
	α+10°, β+10°	**α+10°, β-10°**	**α-10°, β+10°**	**α-10°, β-10°**
J_x-J_z (cm^{-1})	0.38	0.38	0.38	0.38
J_y-J_z (cm^{-1})	-0.17	-0.18	-0.19	-0.18
γ_{ex} (°)	35	34	32	36

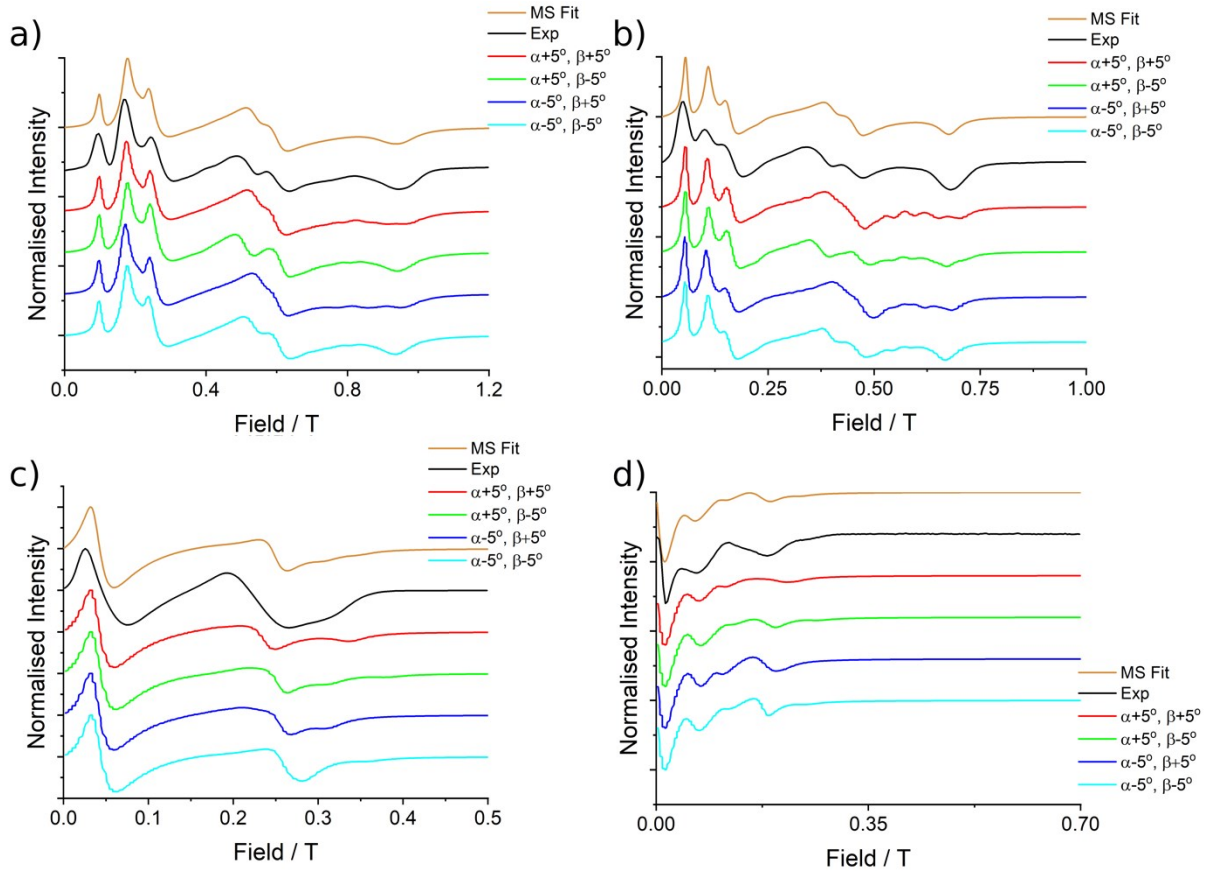

Figure S17. Simulations of **1** using the ±5° parameters in Table S9 compared to experiment (black line) and manuscript simulation (orange line) for **a)** *Q*-band (33.970818 GHz), **b)** *K*-band (23.791 GHz), **c)** *X*-band (9.37198 GHz) and **d)** *S*-band (3.87285 GHz).

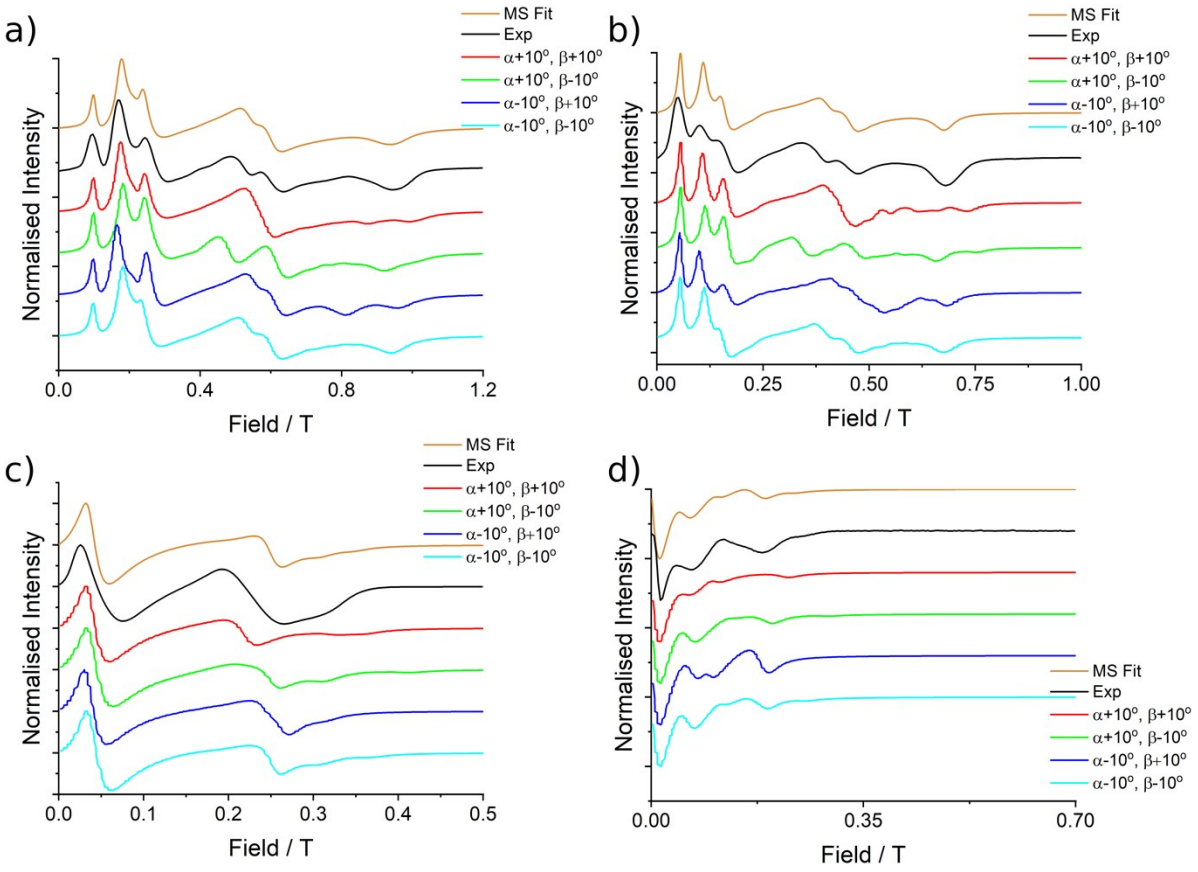

Figure S18. Simulations of **1** using the ±10° parameters in Table S9 compared to experiment (black line) and manuscript simulation (orange line) for **a)** *Q*-band (33.970818 GHz), **b)** *K*-band (23.791 GHz), **c)** *X*-band (9.37198 GHz) and **d)** *S*-band (3.87285 GHz).

Table S10. Fitted parameters for **2** after shifting of g-frame relative to exchange frame by ±5° and ±10°.

	***α*+5°, *β*+5°**	***α*+5°, *β*-5°**	***α*-5°, *β*+5°**	***α*-5°, *β*-5°**
$J_{\perp}$-$J_{\parallel}$ (cm^{-1})	0.069	0.074	0.068	0.075
	***α*+10°, *β*+10°**	***α*+10°, *β*-10°**	***α*-10°, *β*+10°**	***α*-10°, *β*-10°**
$J_{\perp}$-$J_{\parallel}$ (cm^{-1})	0.070	0.088	0.069	0.087

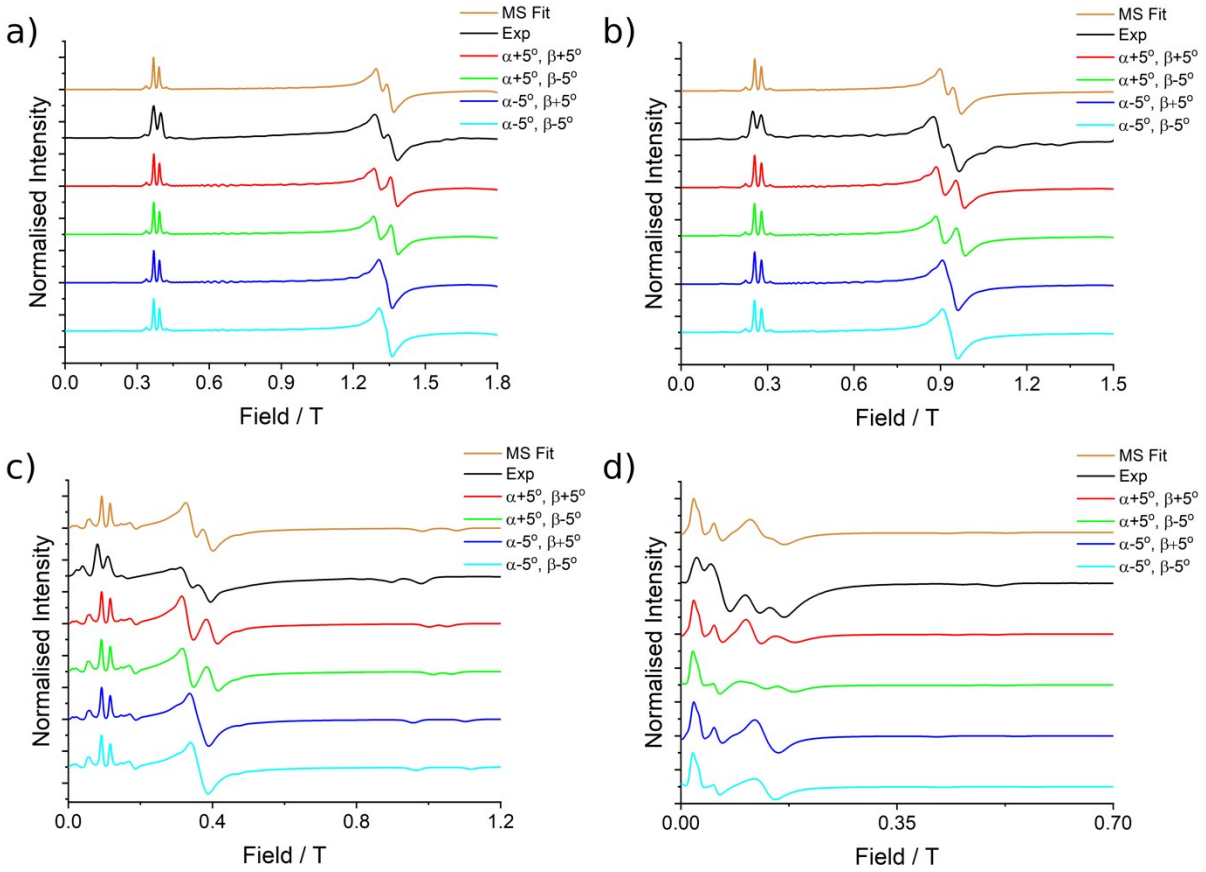

Figure S19. Simulations of **2** using the ±5° parameters in Table S10 compared to experiment (black line) and manuscript simulation (orange line) for **a)** *Q*-band (34.092351 GHz), **b)** *K*-band (23.870 GHz), **c)** *X*-band (9.374342 GHz) and **d)** *S*-band (3.875789 GHz) which show that all simulations are poorer than the simulation presented in the manuscript.

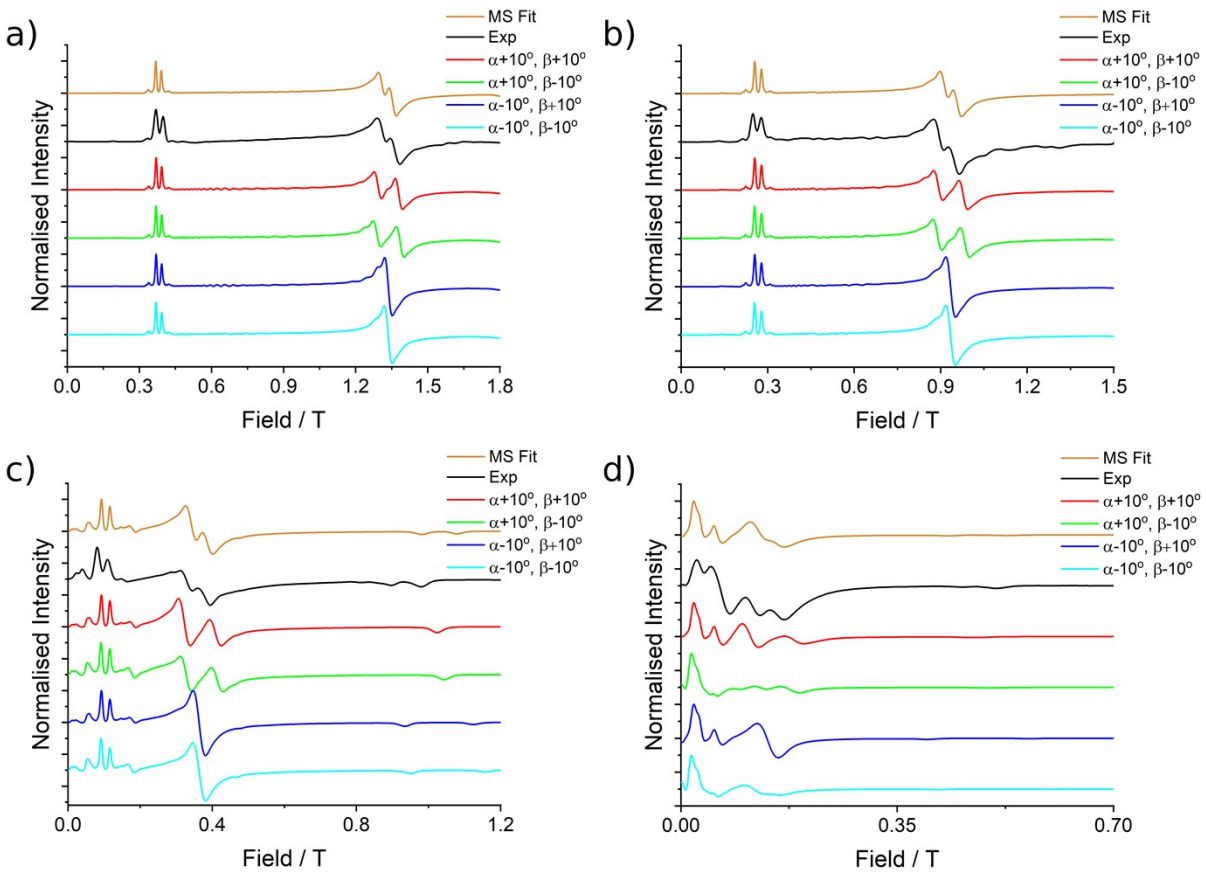

Figure S20. Simulations of **2** using the ±10° parameters in Table S10 compared to experiment (black line) and manuscript simulation (orange line) for **a)** *Q*-band (34.092351 GHz), **b)** *K*-band (23.870 GHz), **c)** *X*-band (9.374342 GHz) and **d)** *S*-band (3.875789 GHz) which show that all simulations are significantly poorer than the simulation presented in the manuscript.

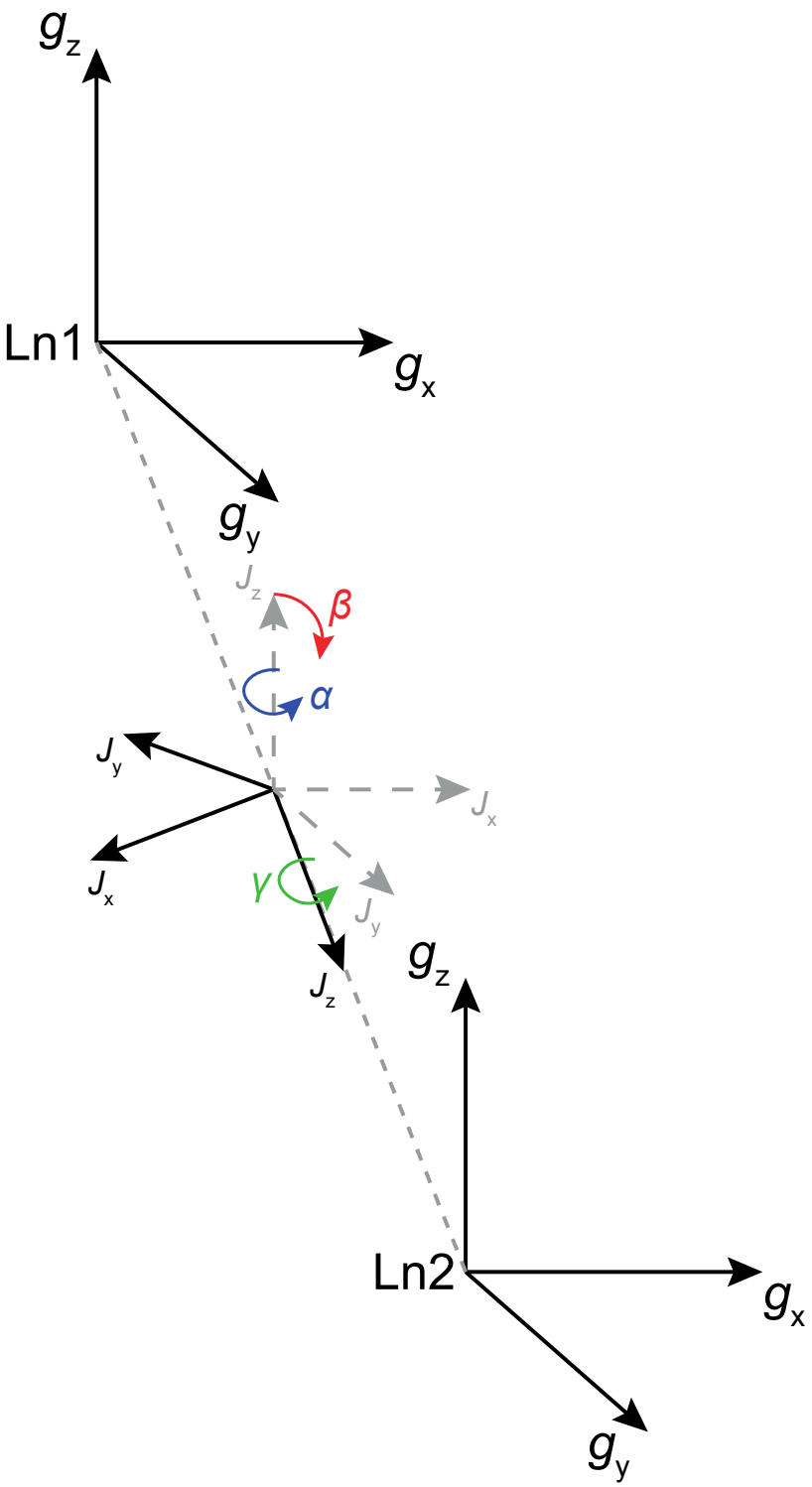

Figure S21. Visualisation of rotation angles of the exchange matrix in the canonical *g*-matrix reference frame.